

A modified moment-fitted integration scheme for X-FEM applications with history-dependent material data

Ziyu Zhang¹ · Wen Jiang² · John E. Dolbow³ · Benjamin W. Spencer²

Received: 25 July 2017 / Accepted: 22 December 2017 / Published online: 29 January 2018
© Springer-Verlag GmbH Germany, part of Springer Nature 2018

Abstract

We present a strategy for the numerical integration of partial elements with the eXtended finite element method (X-FEM). The new strategy is specifically designed for problems with propagating cracks through a bulk material that exhibits inelasticity. Following a standard approach with the X-FEM, as the crack propagates new partial elements are created. We examine quadrature rules that have sufficient accuracy to calculate stiffness matrices regardless of the orientation of the crack with respect to the element. This permits the number of integration points within elements to remain constant as a crack propagates, and for state data to be easily transferred between successive discretizations. In order to maintain weights that are strictly positive, we propose an approach that blends moment-fitted weights with volume-fraction based weights. To demonstrate the efficacy of this simple approach, we present results from numerical tests and examples with both elastic and plastic material response.

Keywords Numerical integration · X-FEM · Internal variables · Moment-fitting

1 Introduction

The eXtended finite element method (X-FEM) was originally developed as a technology to allow discontinuity surfaces to be placed at arbitrary locations inside standard finite elements [1]. This is effected through a combination of enrichment functions and integration schemes. While the X-FEM facilitates the simulation of crack growth with a fixed underlying mesh, the discretization does change as the crack propagates. For application to fracture problems that employ material models with history-dependent properties, such as plasticity models, this necessitates a transfer of state variables between successive discretizations. To date, this issue has not received much attention, as the majority of X-FEM applications have focused on problems in which the bulk response is elastic. In this work, we develop an integration scheme based on

a blending of moment-fitted and volume-fraction weights, which permits state variables to be easily transferred between discretizations as a crack propagates through a mesh.

The X-FEM is based on the partition-of-unity concept, wherein a standard polynomial-based finite element approximation is enhanced with local enrichment functions [2]. The use of enrichment functions that were discontinuous across arbitrary crack surfaces was introduced in Belytschko and Black [3] and Moes et al. [1]. A retrospective on the X-FEM for problems in fracture mechanics was recently provided by Sukumar et al.[4]. In this work, we focus exclusively on the use of Heaviside enrichment that allows for arbitrary discontinuities in the displacement field. The implementation here follows recent work on the X-FEM in which “cut” or “partial” elements are introduced. These are finite elements whose shape functions are standard isoparametric functions but whose element domain does not reside completely within the physical domain of interest. These partial elements usually have two regions that can be delineated as physical and non-physical. Accordingly, quadrature rules need to be designed to integrate functions over the physical portion of the element domain.

In Moes et al. [1], elements intersected by cracks or other surfaces of discontinuity were partitioned into subelements for the purpose of integration. This partitioning allowed for

✉ John E. Dolbow
jdolbow@duke.edu

¹ COMAC Shanghai Aircraft Design and Research Institute, Shanghai 201210, China

² Fuels Modeling and Simulation, Idaho National Laboratory, Idaho Falls, ID 83415-3840, USA

³ Civil and Environmental Engineering, Duke University, Durham, NC 27708-0287, USA

the use of standard Gauss quadrature within the tributary regions on either side of the crack surface, such that the contributions to the linear algebraic system of equations could be accurately integrated. Since that early work, a number of different quadrature strategies have been proposed to address this basic issue. These include replacing the discontinuous functions with an equivalent polynomial [5], the use of Schwarz-Christoffel mappings [6], and, most recently, homogeneous numerical integration (HNI) schemes [7]. In this work, we focus attention on moment-fitting methods, such as those proposed by Sudhakar and Wall [8].

With standard Gauss quadrature, the location and weights of integration points are optimized to integrate functions over a fixed domain of a given shape. Moment-fitting methods allow quadrature rules to be developed to integrate functions over arbitrarily-shaped domains. Essentially, integrals of polynomial functions of a particular order are first calculated with some precision over the physical domain. Then, a system of linear algebraic equations is constructed to solve for the weights of quadrature points such that these same integrals are recovered using a fixed number of quadrature points. In this approach, the accuracy of the moment-fitted quadrature is dictated solely by the number of points, as opposed to both the number of points and their locations. As such it is less efficient than Gauss quadrature, but more flexible in the sense that the same set of points (albeit with different weights) can be used to integrate functions over several different partial domains. This is a great advantage for problems with history-dependent material data stored at integration points. When a crack propagates through an element, the locations of the integration points in the cut elements can be the same as those in the original elements, so material data can be directly copied from the original element's integration points, without the need for complex projection procedures, as would be required when the physical locations of integration points in the cut elements differ from those in the original elements.

Most of the work on the X-FEM for crack growth in elastic-plastic fracture problems has focused on the identification of suitable near-tip enrichment functions, see for example the work of Elguedj et al. [9] and Liu et al. [10]. Fairly little work has focused on the issue of how to deal with the projection of state variables as the crack propagates. Elguedj et al. [9] adopted a two-level strategy of using both fixed and updated quadrature points. The state variables were stored and updated at the fixed integration points, whose locations and weights remained unchanged as the crack propagated. Recently, Martin et al. [11] developed a strategy for X-FEM and cyclic plasticity problems based on replacing the discontinuous enrichment functions with continuous equivalents.

In this work, we develop a simple strategy that permits existing X-FEM implementations to be easily adapted to

problems with bulk plasticity. The method modifies a standard moment-fitting approach by blending the weights with standard Gauss quadrature weights that have been re-scaled by the relative volume fraction of the physical portion of the element domain. The blending is designed to ensure that all weights are strictly positive, such that errors in the tangent stiffness matrix do not give rise to negative eigenvalues. Moreover, the blended weights are able to exactly integrate constant functions, such that a standard linear patch test is satisfied.

This manuscript is outlined as follows. Section 2 describes the problem formulation for both elastic and elastic-plastic crack growth. In Sect. 3, the X-FEM discretization is described, as well as the algorithm for the construction of the blended quadrature weights. A number of numerical examples are presented in Sect. 4 to examine the performance of our proposed strategy. In Sect. 5 we present the conclusion and discuss future endeavors.

2 Problem formulation

Consider a domain $\Omega \subset \mathbb{R}^d$ ($d = 2, 3$) with an internal traction-free crack Γ_c . The complete boundary of the domain is given by $\Gamma = \Gamma_u \cup \Gamma_t \cup \Gamma_c$ with $\Gamma_u \cap \Gamma_t = \emptyset$ (see Fig. 1). Here, Γ_u denotes the portion of the boundary on which displacements are prescribed, while Γ_t is the traction boundary.

The strong form for elastostatics is:

$$\begin{aligned} \nabla \cdot \sigma + b &= \mathbf{0} \text{ in } \Omega, \\ \mathbf{u} &= \bar{\mathbf{u}} \text{ on } \Gamma_u, \\ \sigma \cdot \mathbf{n} &= \bar{\mathbf{t}} \text{ on } \Gamma_t, \\ \sigma \cdot \mathbf{n} &= \mathbf{0} \text{ on } \Gamma_c, \end{aligned} \quad (1)$$

where σ is the Cauchy stress tensor, \mathbf{u} is the displacement, \mathbf{n} is the unit outward normal on the boundary, and \mathbf{b} is the body

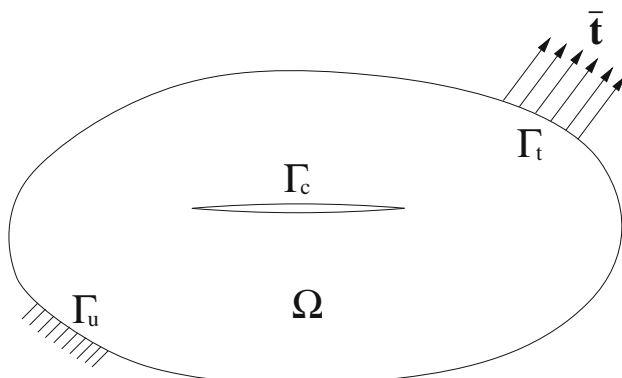


Fig. 1 Problem domain with an internal traction-free crack

force. For the boundary conditions, $\bar{\mathbf{u}}$ and $\bar{\mathbf{t}}$ are the prescribed displacements and tractions on Γ_u and Γ_t , respectively.

The quadrature schemes considered here are applied to several problems to evaluate their applicability to both linear small strain elastic problems and finite deformation plasticity problems. These formulations are both described here.

2.1 Kinematically linear theory

For small-strain elastostatics, a linear strain-displacement relation of the form

$$\boldsymbol{\epsilon} = \frac{1}{2} (\nabla \mathbf{u} + (\nabla \mathbf{u})^T) \quad (2)$$

is employed, and a linear elastic model is used to represent the constitutive relationship between the stress and strain:

$$\boldsymbol{\sigma} = \mathbf{E} : \boldsymbol{\epsilon} \quad (3)$$

where \mathbf{E} is the fourth-order elasticity tensor.

2.2 Kinematically nonlinear theory with plasticity

An incremental approach is followed for finite strain analyses. At each time step, the incremental deformation gradient tensor, $\hat{\mathbf{F}}$ is computed as a function of the coordinates at the current step, \mathbf{x}_{n+1} and at the previous step, \mathbf{x}_n :

$$\hat{\mathbf{F}} = \frac{\partial \mathbf{x}_{n+1}}{\partial \mathbf{x}_n}. \quad (4)$$

To convert this to a form that is convenient for use within an incremental constitutive model, a right polar decomposition is performed on $\hat{\mathbf{F}}$, which is expressed as the product of an incremental rotation $\hat{\mathbf{R}}$ and an incremental right stretch tensor $\hat{\mathbf{U}}$:

$$\hat{\mathbf{F}} = \hat{\mathbf{R}} \cdot \hat{\mathbf{U}} \quad (5)$$

The incremental Cauchy-Green deformation tensor, $\hat{\mathbf{C}}$, is defined below, and can be expressed in terms of $\hat{\mathbf{U}}$ by substituting the decomposed form of $\hat{\mathbf{F}}$ from Eq. 5 and simplifying due to the orthogonality of $\hat{\mathbf{R}}$:

$$\hat{\mathbf{C}} = \hat{\mathbf{F}}^T \cdot \hat{\mathbf{F}} = \hat{\mathbf{U}}^T \cdot \hat{\mathbf{R}}^T \cdot \hat{\mathbf{R}} \cdot \hat{\mathbf{U}} = \hat{\mathbf{U}}^2 \quad (6)$$

thus, $\hat{\mathbf{U}}$ can be computed from $\hat{\mathbf{C}}$ as:

$$\hat{\mathbf{U}} = \hat{\mathbf{C}}^{\frac{1}{2}} \quad (7)$$

which can be evaluated by performing a spectral decomposition of $\hat{\mathbf{C}}$. Once $\hat{\mathbf{U}}$ is known, Eq. 5 is used to compute $\hat{\mathbf{R}}$, and the stretching rate \mathbf{D} is computed as:

$$\mathbf{D} = \frac{1}{\Delta t} \log(\hat{\mathbf{U}}). \quad (8)$$

To avoid the computational cost of performing this spectral decomposition, we follow the approach of Rashid [12], in which Taylor series expansions are used to compute approximations of \mathbf{D} and $\hat{\mathbf{R}}$ which still satisfy strong incremental objectivity.

Once \mathbf{D} and $\hat{\mathbf{R}}$ are available, the constitutive model evaluates the stress for the current step using an incremental form at an intermediate configuration, and then rotates that forward to the new configuration. For elasticity, this can be expressed as:

$$\boldsymbol{\sigma}_{n+1} = \hat{\mathbf{R}} (\boldsymbol{\sigma}_n + \Delta t \mathbf{E} : \mathbf{D}) \hat{\mathbf{R}}^T. \quad (9)$$

This approach permits the use of arbitrary incremental constitutive models to compute the updated stress in the intermediate configuration. The rotation is handled externally to the constitutive model, which computes the updated stress as a function of the strain rate, $\dot{\boldsymbol{\epsilon}} = \mathbf{D}$.

For the bulk constitutive law, we consider classical J_2 plasticity with isotropic hardening [13]. The total strain rate $\dot{\boldsymbol{\epsilon}}$ is additively decomposed into elastic and plastic components, ($\dot{\boldsymbol{\epsilon}}^e$ and $\dot{\boldsymbol{\epsilon}}^p$, respectively):

$$\dot{\boldsymbol{\epsilon}} = \dot{\boldsymbol{\epsilon}}^e + \dot{\boldsymbol{\epsilon}}^p. \quad (10)$$

The stress rate is related to the elastic strain rate through:

$$\dot{\boldsymbol{\sigma}} = \mathbf{E} : \dot{\boldsymbol{\epsilon}}^e \quad (11)$$

The admissible space for the stress field is given by a von Mises yield condition of the form

$$(\boldsymbol{\sigma}, \alpha) = ||\text{dev}[\boldsymbol{\sigma}]|| - \sqrt{\frac{2}{3}} K(\alpha) \leq 0 \quad (12)$$

where $\text{dev}[\cdot]$ denotes the deviatoric part of the tensor, and α is the equivalent plastic strain, used as an internal state variable to define the linear hardening behavior:

$$K(\alpha) = \sigma_Y + \bar{K}\alpha \quad (13)$$

where σ_Y is the yield stress and \bar{K} is the hardening modulus. The plastic strain increment is expressed as the product of the plastic multiplier λ and the flow direction \mathbf{m} , which is the outward normal of the yield surface in the case of associated flow, which is assumed here.

$$\dot{\boldsymbol{\epsilon}}^p = \dot{\lambda} \mathbf{m}. \quad (14)$$

The equivalent plastic strain rate is related to the plastic multiplier by:

$$\dot{\alpha} = \sqrt{\frac{2}{3}} \dot{\lambda}. \quad (15)$$

When the trial elastic stress exceeds the yield criterion, a return mapping procedure is used to obtain a value of $\dot{\lambda}$ that satisfies the conditions outlined above.

2.3 Weak form

The weak form of the boundary-value problem in (1) is: find $\mathbf{u} \in \mathcal{U}$ such that

$$\int_{\Omega} \boldsymbol{\sigma} : \delta \boldsymbol{\epsilon} d\Omega = \int_{\Omega} \mathbf{b} \cdot \delta \mathbf{u} d\Omega + \int_{\Gamma_t} \bar{\mathbf{t}} \cdot \delta \mathbf{u} dS \quad \forall \delta \mathbf{u} \in \mathcal{U}_0, \quad (16)$$

where \mathcal{U} and \mathcal{U}_0 are the trial space for the displacement field and the test space (virtual displacements), respectively. The trial and test spaces admit functions that are discontinuous across Γ_c .

3 Discretization

3.1 Approximation

The weak form is recast in finite-dimensional spaces $\mathcal{U}^h \subset \mathcal{U}$ and $\mathcal{U}_0^h \subset \mathcal{U}_0$. The extended finite-element approximation to the displacement field is given by

$$\mathbf{u}^h(\mathbf{x}) = \sum_I \phi_I(\mathbf{x}) \mathbf{u}_I \quad (17)$$

in terms of the nodal shape functions ϕ_I and degrees of freedom \mathbf{u}_I , and where the sum is over all nodes I in the mesh.

We follow the work of Richardson et al [14] to build an approximation \mathbf{u}^h that allows for discontinuities in the displacement field across an embedded crack geometry. Given a crack geometry superimposed on top of a background finite element mesh, this approach builds the approximation (17) in two steps. In the first step, multiple copies of every element intersected by the crack are created, one for each disjoint material region. In the second step, nodes are condensed between elements sharing material on common edges. While the algorithm described in Richardson et al [14] was originally developed for triangular elements, it has been adapted in this work for isoparametric quadrilateral elements. For simplicity, we also impose the restriction that cracks must terminate on element edges.

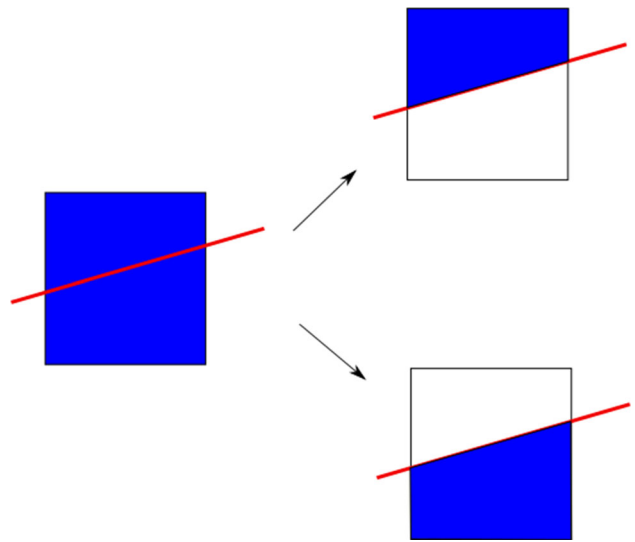


Fig. 2 A parent element (left) intersected by a crack (in red) is partitioned into two children, or partial elements (right). The two overlapping copies of the original element have disjoint physical regions (also called fragments), which are marked by the shaded blue areas. (Color figure online)

For elements cut by the interior of the crack, sufficiently far away from the crack tip, the algorithm essentially results in two copies, or “children” from a single “parent” element, one on each side of the crack surface, as shown in Fig. 2. Each child or “partial element” contains two portions, a physical portion and a non-physical (or void) portion, and consist of real and phantom nodes. The nodal shape functions ϕ_I for partial elements are identical to those employed in standard, intact elements. The new discretization is constructed as needed at the end of a time step, before the loads are incremented. After construction, any newly-created displacement degrees of freedom in partial elements inherit their values from the corresponding nodes in the original, intact element. This insures that the displacement field over each of the partial regions is identical to what it was in the original element at the conclusion of the time step.

In partial elements, contributions to the tangent stiffness matrix and internal force vector are assembled by integrating only over the physical portion. In the current work, this is effected by changing the weights of quadrature points, as detailed in the following section.

3.2 Integration

Standard finite-element quadrature rules approximate an integral over an element via

$$\int_{\Omega^e} f d\mathbf{v} \approx \sum_{g=1,n} W_g f(\mathbf{x}_g) \quad (18)$$

corresponding to a linear combination of function evaluations at each of the n quadrature points \mathbf{x}_g , scaled by the weights W_g .

With Gaussian quadrature, both the coordinates \mathbf{x}_g of the integration points and the weights W_g are optimized to allow the highest order polynomial to be exactly integrated for a given number of points. To integrate fields over partial elements such as those shown in Fig. 2, one option is to repartition the physical side of the element into a set of “subelements” that can be used for integration. While this approach is effective, it requires the generation of a new set of quadrature points and state-variable remapping.

In this manuscript, we adopt an alternative approach. When an element is split into two partial elements as shown in Fig. 2, each copy of the element is given the same number of quadrature points (in the same locations), as the original, intact element. State variables are directly copied from the original element values at the quadrature points to the new ones in the partial elements. In addition to the aforementioned transfer of displacement degrees of freedom, this insures that all fields in the physical regions in the new discretization are identical to those in the previous discretization.

After the transfer, the weights of the quadrature points in each newly-created partial elements are recalculated in order to be able to accurately integrate fields over the physical domains. We now describe two different types of weights for use in partial elements: moment-fitted weights W_g^m and volume-fraction adjusted weights W_g^v . An approach which blends these two types of weights together is also described in Sect. 3.2.1.

Moment-fitting is a well-known method to construct quadrature rules for partial elements [15]. The general form of the equations reads

$$\left\{ \begin{array}{l} \int_{\Omega} \phi_1(\mathbf{x}) d\mathbf{x} \\ \int_{\Omega} \phi_2(\mathbf{x}) d\mathbf{x} \\ \vdots \\ \int_{\Omega} \phi_m(\mathbf{x}) d\mathbf{x} \end{array} \right\} = \left[\begin{array}{cccc} \phi_1(\mathbf{x}_1) & \phi_1(\mathbf{x}_2) & \cdots & \phi_1(\mathbf{x}_n) \\ \phi_2(\mathbf{x}_1) & \phi_2(\mathbf{x}_2) & \cdots & \phi_2(\mathbf{x}_n) \\ \vdots & \vdots & \vdots & \vdots \\ \phi_m(\mathbf{x}_1) & \phi_m(\mathbf{x}_2) & \cdots & \phi_m(\mathbf{x}_n) \end{array} \right] \left\{ \begin{array}{l} w_1 \\ w_2 \\ \vdots \\ w_n \end{array} \right\} \quad (19)$$

for integrating a set of m basis functions using a set of n quadrature points. In the above, Ω denotes the physical domain of a partial element and $\{\mathbf{x}_g\}_{g=1}^n$ are the physical coordinates of n predefined quadrature points. A standard four-noded quadrilateral element often employs four Gaussian quadrature points. If these same points were to be used in a moment-fitting algorithm, then $n = 4$. While four Gauss quadrature points can prove sufficient to accurately integrate an element stiffness matrix over an intact element, they will generally be insufficient to accurately integrate the

same matrix over an arbitrary partial region. As described in Sect. 3.2.2, employing a six-point integration rule ($n = 6$) permits the use of an expanded set of basis functions to more accurately integrate the bilinear functions employed in isoparametric linear finite elements over arbitrary physical regions. For these cases, the basis functions ϕ_i are

$$\{\phi_i\}_{i=1}^4 = [1, x, y, xy]^T \quad \text{for } m = 4, \quad (20)$$

and

$$\{\phi_i\}_{i=1}^6 = [1, x, y, x^2, xy, y^2]^T \quad \text{for } m = 6 \quad (21)$$

In this manuscript, we will set $m = n$ with either the four-point or the six-point rule, such that (19) is a linear system that can readily be solved by directly inverting the square coefficient matrix.

In moment-fitting approaches, the left side of (19) also needs to be determined in some manner. The approach we adopt here is to approximate those integrals with quadrature over a set of subelements that are constructed only for this purpose. Such subelements, as shown in Fig. 3, are identical to those constructed in the original instantiation of the XFEM [1]. Considering that in the current method the crack within an element is always represented by a straight line, the partial element is essentially a polygon with three, four or five vertices. For triangular or quadrilateral shaped subdomains, standard three or four point Gaussian quadrature rules can be employed. Pentagonal regions are partitioned into a set of five triangular regions, as shown in Fig. 3.

As indicated in Fig. 3, a third order Gaussian quadrature rule is used in the partial elements to integrate the basis functions (27) up to the second order. Therefore, the quadrature used to calculate the left hand side of (19) gives exact integral values.

The volume fraction approach is a simple alternative to moment fitting. Integration point weights W_g^v are simply formed by re-scaling the original Gaussian weights W_g based on the ratio of the partial element volume (or area in two dimensions) to the original element volume. Let V_e denote the total element volume and V_e^P the volume of the physical portion of the partial element. Volume fraction weights are then calculated as:

$$W_g^v = \frac{V_e^P}{V_e} W_g. \quad (22)$$

This is equivalent to the special case in the moment fitting equation (19) for which $m = 1$ and $\phi_1 = 1$, so a constant function is evaluated exactly over a partial element with this approach. While these weights are not particularly accurate for integrating higher-order functions, it is worth noting that they are strictly positive and this will prove beneficial for

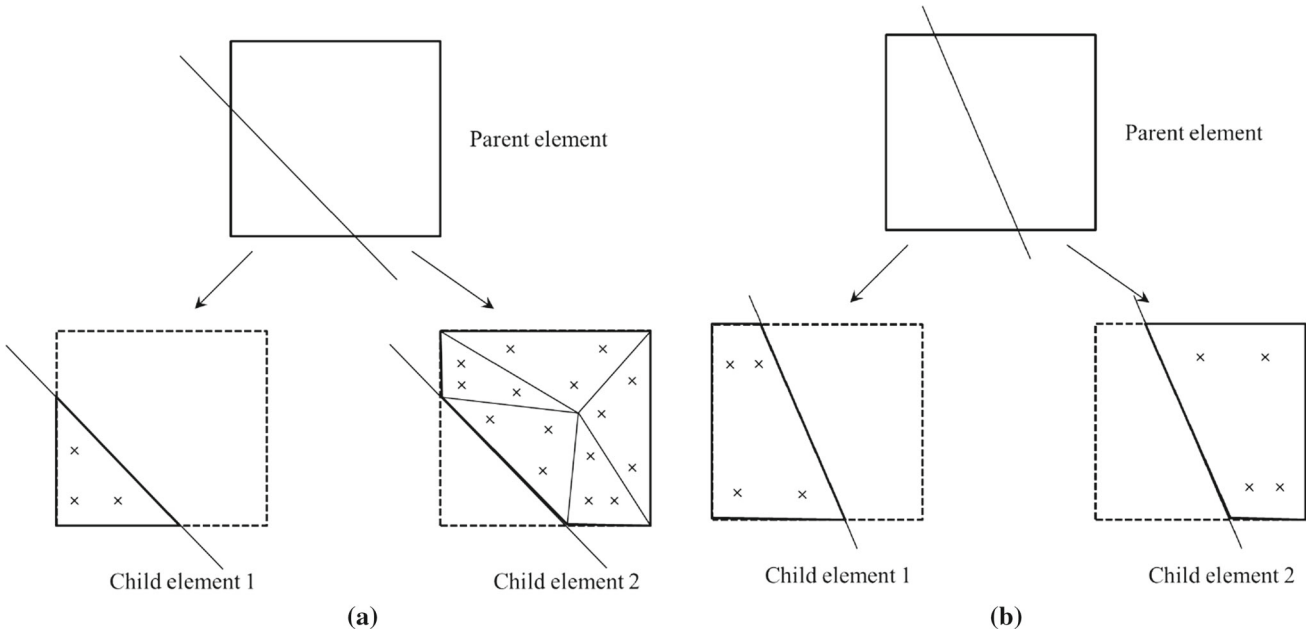


Fig. 3 The Gaussian points used to integrate the left hand side of (19). In Case 1, the physical domains of the two child elements are a triangle and a pentagon, respectively. The triangle uses a three-point Gaussian quadrature rule with third order exactness and the pentagon is triangulated so that each sub-triangle is using the same rule. In Case 2, both physical domains are quadrilaterals and a four-point Gaussian rule is used to achieve third order exactness for numerical integration. **a** Case 1 of a cut quad element. **b** Case 2 of a cut quad element

the construction of blended weights. We note that a basic volume-fraction weight approach has been used before in X-FEM calculations, such as in Song et al. [16].

3.2.1 Blended weights

While the moment-fitted weights are in general more accurate than volume fraction weights, there are no guarantees that they will be positive. In fact it is quite common to encounter negative weights in one or more integration points of a cut element, especially when the physical volume fraction of that element is small. An example of such a case is shown in Sect. 4.2 of this paper. These negative weights can give rise to negative eigenvalues for the stiffness matrices, which in turn can trigger a lack of convergence in the Newton algorithm to solve the nonlinear system of equations. By contrast, the volume-fraction adjusted weights are always positive. We have devised a new algorithm that blends the two weights together to create new weights W_g^b that are guaranteed to be strictly positive.

The idea is to find a scale parameter $0 \leq \alpha^e \leq 1$ that is constant over each element to blend the two together as

$$W_g^b = (1 - \alpha^e)W_g^v + \alpha^e W_g^m \quad (23)$$

such that we satisfy the constraint:

$$W_g^b \geq 0 \quad \forall g. \quad (24)$$

Solving for the largest value of α_g to satisfy this condition yields

$$\alpha_g = \frac{-W_g^v}{W_g^m - W_g^v}. \quad (25)$$

Note that both the numerator and denominator should be negative here, so strictly positive values for the ratio result. Then we set

$$\alpha^e = \min_g \alpha_g, \quad (26)$$

which guarantees that all blended weights are strictly positive.

3.2.2 Six-point quadrature rule

The reason for our interest on the six-point quadrature rule lies in its ability to accurately integrate the stiffness matrix for linear elastic problems with a structured mesh. For a structured mesh that uses linear shape functions, each entry of the element stiffness matrix \mathbf{k}^e is a polynomial up to the second order. Since any second-order polynomial in two dimensions contains the following six basis functions

$$[1, x, y, x^2, xy, y^2], \quad (27)$$

Table 1 Option 1 for six-point rule

	ξ	η	w
1	0.0000000000000000	0.0000000000000000	1.142857142857140
2	0.0000000000000000	0.966091783079296	0.439560439560440
3	0.851914653304601	0.455603727836193	0.566072207007532
4	-0.851914653304601	0.455603727836193	0.566072207007532
5	0.630912788976754	-0.731629951573135	0.642719001783677
6	-0.630912788976754	-0.731629951573135	0.642719001783677

Table 2 Option 2 for six-point rule

	ξ	η	w
1	0.0000000000000000	-0.356822089773090	1.286412084888850
2	0.0000000000000000	0.934172358962716	0.491365692888926
3	0.774596669241483	0.390885162530071	0.761883709085613
4	-0.774596669241483	0.390885162530071	0.761883709085613
5	0.774596669241483	-0.852765377881771	0.349227402025498
6	-0.774596669241483	-0.852765377881771	0.349227402025498

it is expected that six predefined quadrature points are needed in order to achieve the highest exactness by solving (19).

In Wissmann and Becker [17], a method to determine partially symmetric quadrature formulas for regions with the same or higher symmetries is introduced. The key idea is to reduce the moment equation system based on the a priori assumption of the structure of a formula. This method is especially useful to achieve even degrees of exactness for quadrature rules which exhibit only partial symmetry. The resulting moment fitting system is solved numerically and a couple of schemes which achieve the exactness in the order of four, six and eight are obtained. In this work we omit the detailed mathematical derivation and only present in Tables 1 and 2 the results of the two six-point rules proposed in [17]. Figure 4 schematically shows the positions of the six quadra-

ture points in the parent domain of a quadrilateral element. In this work since there is no reason to preferably use either of these two options, we consistently choose Option 1 in our moment-fitting approach.

3.3 Assembly

The discretized form of the weak boundary-value problem (16) is solved using standard finite element procedures to assemble the contributions of individual elements e :

$$\sum_e \int_{\Omega^e} (\mathbf{B}^e)^T \boldsymbol{\sigma} d\Omega = \sum_e \int_{\Omega^e} (\mathbf{N}^e)^T \mathbf{b} d\Omega + \sum_e \int_{\Gamma_i^e} (\mathbf{N}^e)^T \bar{\mathbf{t}} dS \quad (28)$$

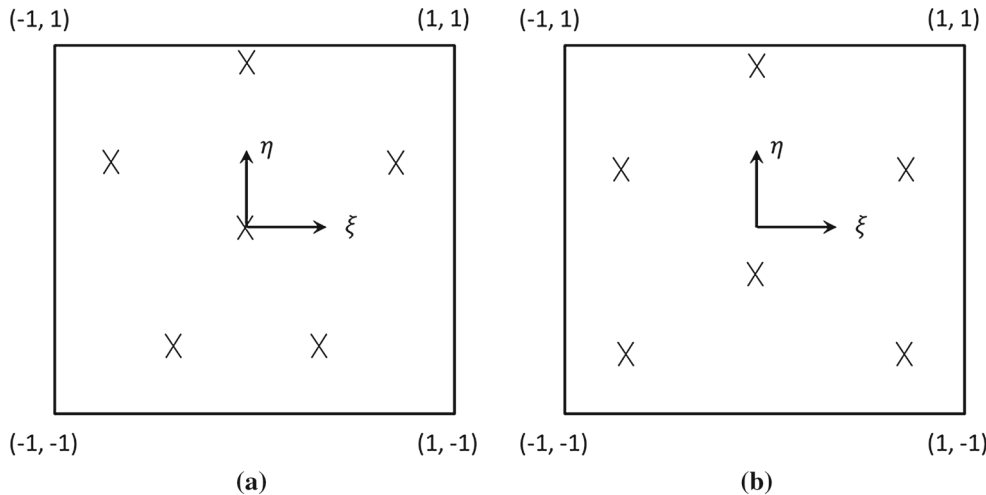


Fig. 4 The two six-points quadrature rule proposed by Wissmann and Becker [17]. **a** Option 1. **b** Option 2

where \mathbf{N}^e is the vector of finite element shape functions and \mathbf{B}^e is the displacement-strain operator, expressed as follows for two dimensional quadrilateral elements:

$$\mathbf{B}^e = [\mathbf{B}_1^e \ \mathbf{B}_2^e \ \mathbf{B}_3^e \ \mathbf{B}_4^e], \quad \mathbf{B}_i^e = \begin{bmatrix} N_{i,x}^e & 0 \\ 0 & N_{i,y}^e \\ N_{i,y}^e & N_{i,x}^e \end{bmatrix}. \quad (29)$$

For the case of small-strain elasticity, the elemental stiffness matrix reads

$$\mathbf{k}^e = \int_{\Omega^e} (\mathbf{B}^e)^T \mathbf{E} \mathbf{B}^e d\Omega. \quad (30)$$

Once the cutting algorithm has been applied to split cut elements into partial elements with appropriate connectivity, the only modification to this standard procedure for Heaviside-enriched X-FEM is that the modified quadrature weights discussed in Sect. 3.2 are employed to integrate partial elements. For problems where volumetric locking is a concern, additional steps are taken as described in the next section.

3.3.1 Volumetric locking

With J_2 plasticity, plastic flow is purely distortional. In order to alleviate any potential mesh locking with low-order elements, in this work we adopt a variation of the $\bar{\mathbf{B}}$ approach [18]. In particular, we employ the approach described in [19], which uses a modified deformation gradient, $\bar{\mathbf{F}}$. We emphasize that this approach is only used for those examples in Sect. 4 in which nearly-incompressible behavior is anticipated.

The deformation gradient \mathbf{F} can be multiplicatively decomposed into volumetric (\mathbf{F}^{vol}) and deviatoric (\mathbf{F}^{dev}) components as follows:

$$\mathbf{F} = \mathbf{F}^{vol} \mathbf{F}^{dev} \quad (31)$$

where the volumetric and deviatoric components are defined as:

$$\mathbf{F}^{vol} = J^{\frac{1}{3}} \mathbf{I}, \quad (32)$$

$$\mathbf{F}^{dev} = J^{-\frac{1}{3}} \mathbf{F}, \quad (33)$$

in which $J = |\mathbf{F}|$. A volume-averaged J for the full element, termed \bar{J} is computed as:

$$\bar{J} = \frac{\int_{V_e} J dV}{V_e}. \quad (34)$$

In partial elements, V_e denotes the volume of the physical portion of the element. In partial elements, the moment fitting

weights or volume fraction approach is used to integrate \bar{J} . \bar{F} can then be computed directly for integration point g as:

$$\bar{\mathbf{F}}_g = \left(\frac{\bar{J}}{J_g} \right)^{\frac{1}{3}} \mathbf{F}_g. \quad (35)$$

The stress is computed as a function of $\bar{\mathbf{F}}$, while the transpose of $\bar{\mathbf{B}}$ is used to compute the divergence of the stress in (28). For a given integration point g , $\bar{\mathbf{B}}$ is defined as:

$$\bar{\mathbf{B}}_g = \mathbf{B}_g - \mathbf{B}_g^{vol} + \bar{\mathbf{B}}^{vol} \quad (36)$$

where \mathbf{B}^{vol} is the volumetric portion of \mathbf{B} , and the element averaged $\bar{\mathbf{B}}^{vol}$ is computed as:

$$\bar{\mathbf{B}}^{vol} = \frac{\int_{V_e} \mathbf{B}^{vol} dV}{V_e}. \quad (37)$$

The same integration procedure described above for computing \bar{J} in the X-FEM is used for $\bar{\mathbf{B}}^{vol}$.

4 Numerical examples

This section presents numerical studies in which results obtained using the quadrature rules described previously are compared to assess the relative accuracy of the various schemes. All cases shown here are two-dimensional models with 4-node, bilinear quadrilateral elements. Comparisons are made between four-point and six-point quadrature rules with weights obtained through moment fitting, the volume fraction strategy, the blended approach, and a reference case based on a high-order modified Gauss-Lobatto rule. The problems considered here include tests of a single quadrilateral element, three small-strain linear elastic tests and one test with finite deformation elasto-plasticity.

4.1 Stiffness matrix error for a single element

A study is performed on a single element cut into two partial elements to assess the error in the stiffness matrix associated with the various integration schemes. For each integration scheme, the errors in the stiffness matrices for the two partial elements are evaluated, as well as the error in the stiffness matrix of the full original element, obtained by assembling the matrices of the two partial elements together. In all cases, results are compared to a reference stiffness matrix \mathbf{k}_{ref} , and a relative error is computed based on an L_2 norm:

$$\text{error} = \frac{||\mathbf{k}_{diff}||_{L_2}}{||\mathbf{k}_{ref}||_{L_2}} \quad (38)$$

where k_{diff} is the absolute difference between the matrix of interest and the reference matrix k_{ref} .

In computing the error for the full original element, k_{ref} is computed using a standard nine-point, 3×3 Gauss quadrature rule on the original, un-cut element. A 2×2 Gaussian rule is sufficient to exactly integrate undistorted quadrilateral elements, but introduces slight errors for distorted elements due to the presence of rational terms. The higher order, 3×3 scheme is thus employed to provide a slightly more accurate reference solution. For the partial elements, k_{ref} is obtained by integrating over the sub-elements in the triangulated sub-domains, using a three-point Gauss quadrature rule for each sub-element as shown in Fig. 3a.

The error in the stiffness matrix is computed for both a regular element and a distorted element, as shown in Fig. 5. The undistorted element is a square with nodes at $(0, 0)$, $(1, 0)$, $(1, 1)$ and $(0, 1)$, while the distorted element has nodes at $(1, 1)$, $(2, 1)$, $(2.5, 2.5)$ and $(1, 2)$. The elasticity parameters $E = 2000$ and $\nu = 0.3$ are used in this study. For both element configurations, the error in the stiffness matrix is computed for a variety of crack orientations. As shown in Fig. 5, one side of the crack always intersects with the middle of Side 1, while the other intersection point is swept along Side 4. The relative error in the stiffness matrices is plotted as a function of the position of the intersection of the crack with Side 4.

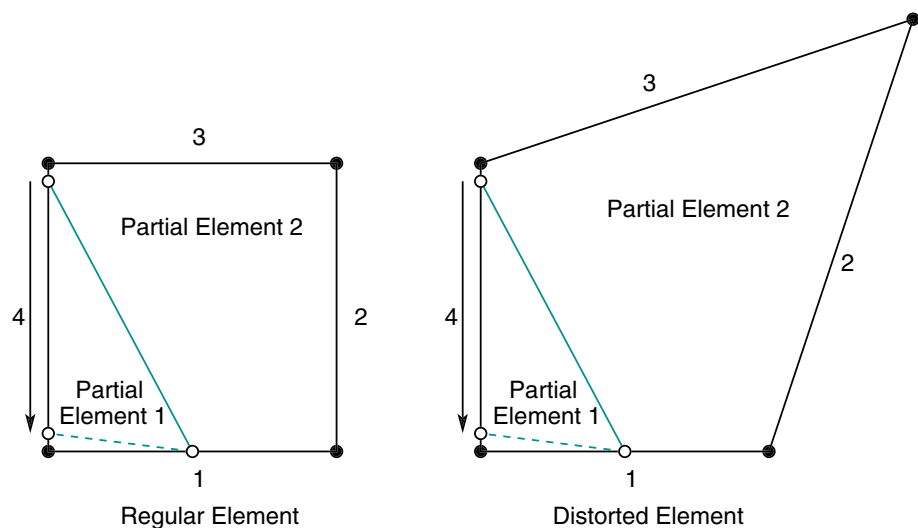
To demonstrate the effect of the blending strategy described in Sect. 3.2.1, the stiffness matrices were evaluated using the moment fitting integration scheme both with and without blending. In the case with blending, the weights were adjusted if negative weights were encountered. In the case without blending, the weights obtained through moment fitting were used to evaluate the stiffness, even if the weights at one or more integration points were negative. Figure 6 shows the error in the stiffness as a function of the posi-

tion of the intercept on Side 4 for the case without blending, while Fig. 7 shows equivalent results when blending is used. Errors in the stiffness matrix are shown for both full and partial elements. For the full element, errors are calculated for both moment fitting schemes, as well as for a “sub-element integration” scheme that integrates over the full element using the union of the triangulated sub-domains shown in Fig. 3.

Multiple observations can be made from these results:

- All of the integration schemes considered here exactly integrate the full un-distorted element when blending is not used. The 4-point and 6-point rules can both exactly integrate the stiffness matrix for an undistorted element because it is only a function of 2nd order polynomials.
- Small but nonzero errors can be seen in the integration of the distorted full element using both moment-fitting schemes, as well as sub-element integration. This is due to the inability of these schemes to exactly integrate the rational terms that appear in distorted elements. The 6-point rule gives the most accurate solution, followed by integration over the triangulated sub-elements and the 4-point rule.
- When blending is not used, the 6-point rule exactly integrates the two partial elements obtained from the regular element. This is because the 6-point rule exactly integrates all terms in the 2nd order polynomials that are used to form the stiffness matrix, and the 6 points correspond to the 6 terms in the 2nd order polynomial used in the moment fitting procedure. Because the 4-point rule does not permit including the x^2 and y^2 terms in moment fitting, its accuracy suffers.
- When blending is not used, the smallest errors are for the 6-point rule with moment fitting, followed by the 4-point rule with moment fitting, and finally by the volume

Fig. 5 Cut quadrilateral elements used to evaluate errors in the stiffness matrix showing the undistorted (left) and distorted (right) cases. The orientation of the crack surface is varied by changing the location of the intercept along side 4, while the intercept in the middle of side 1 is held fixed



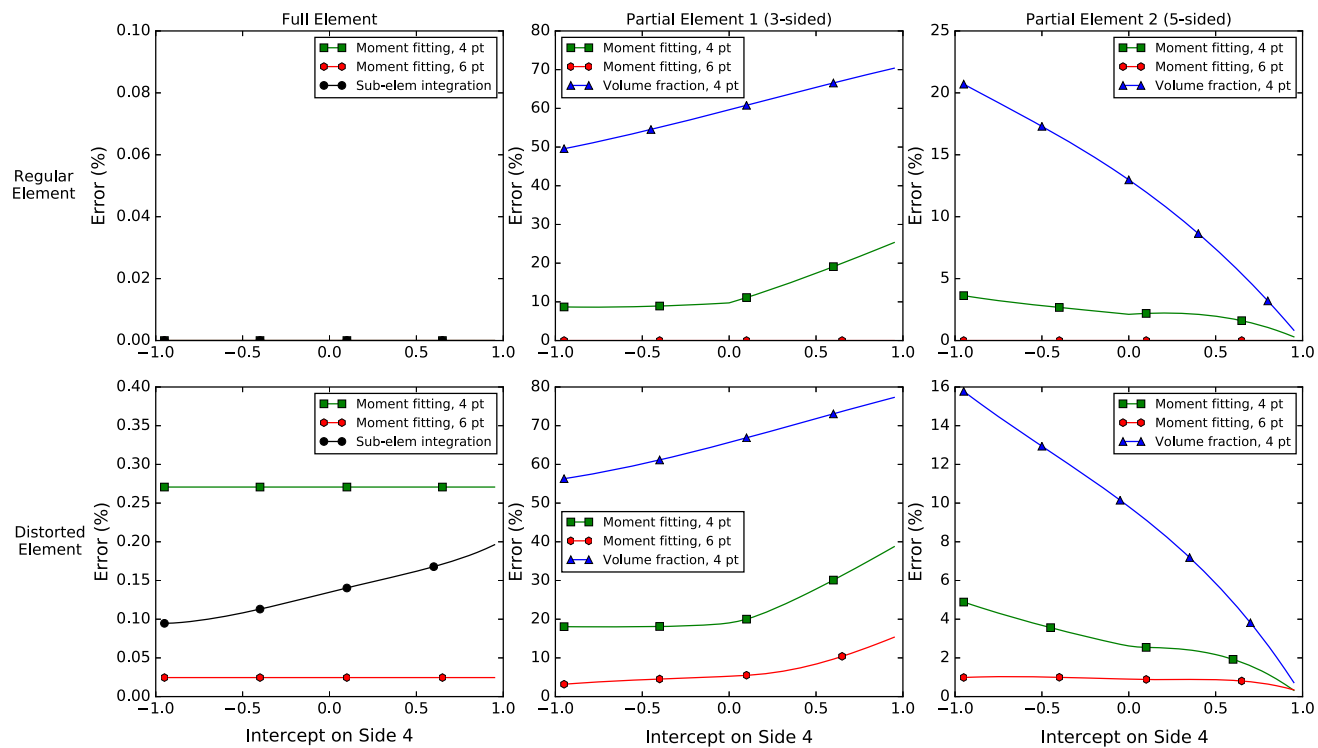


Fig. 6 Error in the stiffness matrix as a function of the crack intercept with Side 4 for the single element in Fig. 5 using various integration schemes. Moment fitting weights are not modified in this case, even if they are negative. This shows the errors for integration of the full original element (left) and the two partial elements (center and right) for both the regular (top) and distorted (bottom) elements

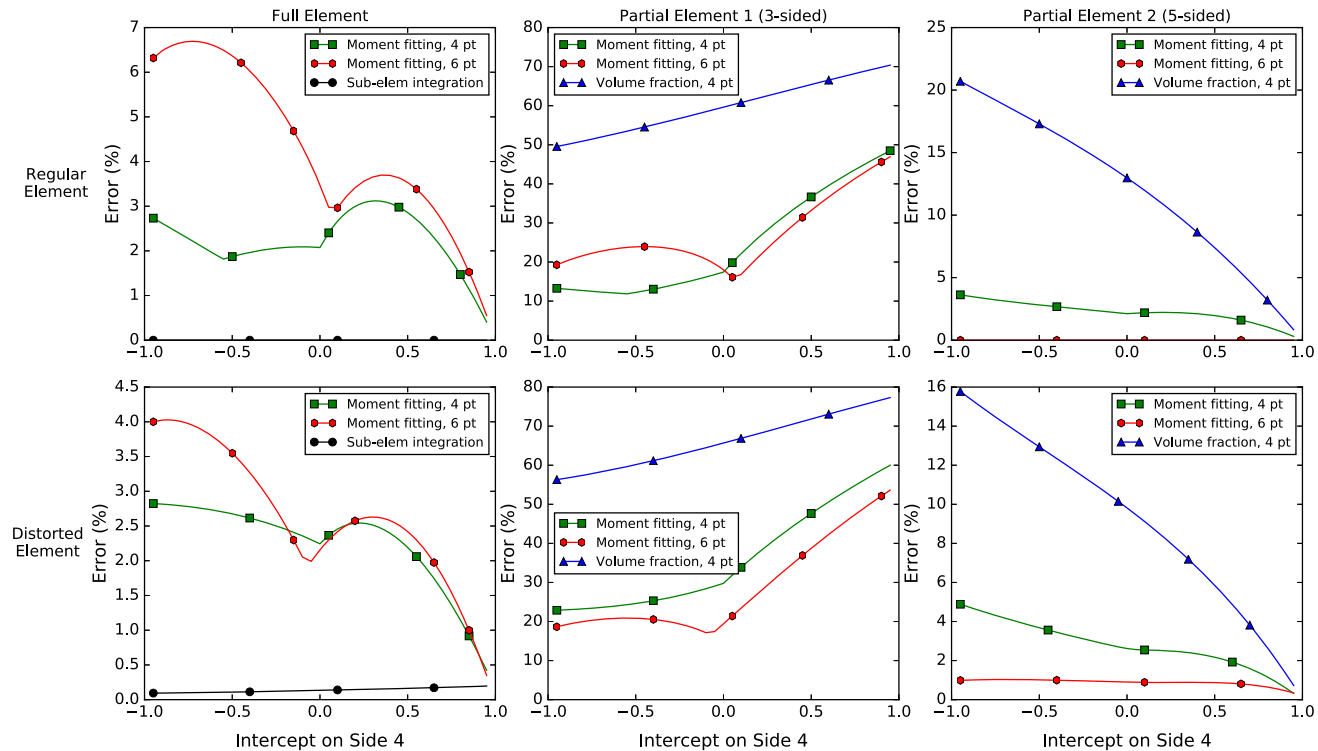


Fig. 7 Error in the stiffness matrix as a function of the crack intercept with Side 4 for the single element in Fig. 5 using various integration schemes. Moment fitting weights are blended with volume fraction weights to avoid negative weights. This shows the errors for integration of the full original element (left) and the two partial elements (center and right) for both the regular (top) and distorted (bottom) elements

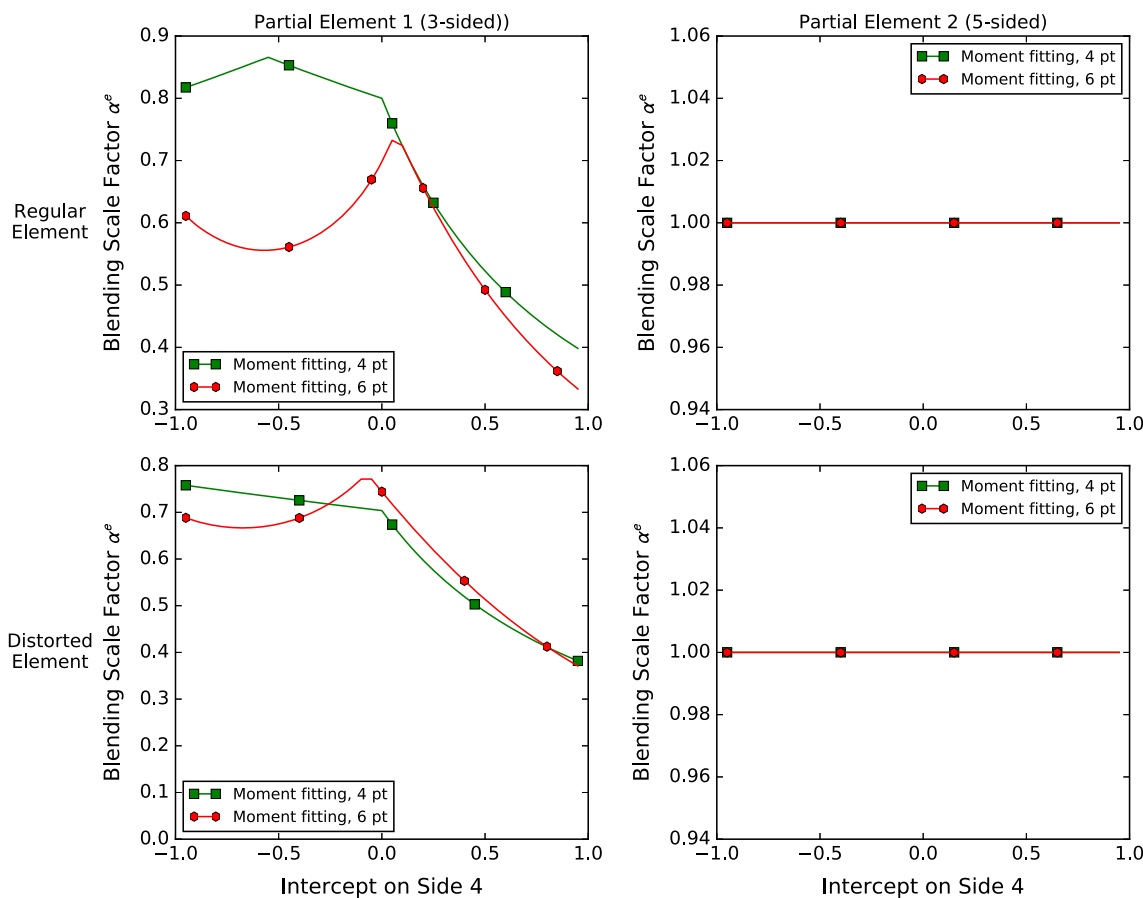


Fig. 8 Blending factor α^e as a function of the crack intercept with Side 4 for the two partial elements obtained from the original single element when blended weights are used with moment fitting. Results are shown for partial elements 1 (left) and 2 (right) for both the regular (top) and distorted (bottom) elements

fraction method with a 4-point rule. The moment fitting technique and the 6-point rule both provide significantly improved accuracy over the base 4-point rule case, for both the regular and distorted element.

- When moment fitting is used, the 3-sided partial element (Partial Element 1) has at least one quadrature point with a negative weight for both the 4-point and the 6-point rule with moment fitting, and as a result, when the blending strategy is used, the blending factor α^e is between 0 and 1 (Fig. 8). The 5-sided partial element does not have any negative weights, so the pure moment fitting weights are used. When blending is activated, the errors with moment fitting are still significantly lower than for the volume fraction scheme, but the errors for the 6-point rule are very similar to those for the 4-point rule, rather than much lower, as they are without blending.

Results similar to those for the crack intercepting Side 4 at varying locations have also been computed for a crack intercepting varying points on Sides 2 and 3, with the same interception point on Side 1. These results are not shown here

for the sake of brevity. The errors shown here for Side 4 are very representative of those for Sides 2 and 3, which have similar magnitudes of error and show the same trends as for this case.

4.2 Negative eigenvalue issue in beam bending example

As shown in the previous section, using the blending procedure to eliminate negative integration point weights obtained through moment fitting increases errors in the stiffness matrix of cut elements, although those errors are still significantly lower than those for the volume fraction method. The tradeoff for the loss of accuracy with blended weights is an increase in solution robustness. Numerous convergence issues were encountered in the nonlinear solution process for the finite strain plasticity problem shown later in this paper with both iterative and direct solvers when the unmodified moment fitting weights (which were negative at some integration points) were used, while those problems were completely eliminated when the blending strategy was used.

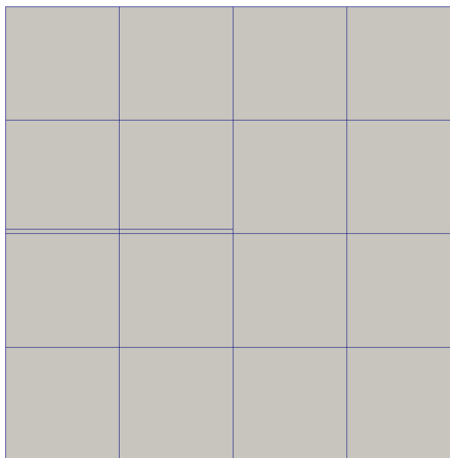


Fig. 9 Mesh used to demonstrate negative eigenvalue issue for beam bending example

The small model shown in Fig. 9 is useful to demonstrate the effects of negative weights on the eigenvalues of a system, as discussed in Sect. 3.2.1. A uniform 4×4 mesh of a square domain from $(0.0, 0.0)$ to $(1.0, 1.0)$ comprised of linear four-noded quadrilateral elements is cut by a crack from the point $(0.0, 0.51)$ to $(0.5, 0.51)$. The crack is intentionally located close to an element edge because that is expected to result in negative weights in the standard moment-fitting approach. In this model, elastic constants $E = 10^6$ and $\nu = 0.3$ are used with plane strain conditions. Dirichlet boundary conditions are imposed on horizontal displacements on the left side, and on vertical displacements on the bottom side of this model.

With the standard moment-fitting approach and a four-point quadrature rule, negative weights of -0.0265 are obtained at two quadrature points for each of the partial elements with smaller physical domains (four quadrature points in total). The corresponding stiffness matrix has one negative eigenvalue of -570.1812 . While negative eigenvalues do not necessarily prevent obtaining a solution, they can make it significantly more difficult. For example, the linear system of equations obtained from this example was solved in MATLAB's [20] Generalized minimum residual (GMRES) solver, with options of `restart = 10` and `tol = 1.0e-12`. A converged result was obtained in 7152 iterations. On the other hand, the blended-weights approach eliminates the negative weights and does not produce any negative eigenvalues in the stiffness matrix. For the same discrete problem and solver settings, the use of blended weights gave rise to a system that converged in only 377 iterations. This clearly demonstrates that while negative weights will not necessarily preclude obtaining a converged solution, they are problematic and pose potential convergence issues for linear and nonlinear systems of equations. For this reason, the blending approach is used in all of the X-FEM moment fitting solutions shown in the remainder of this manuscript.

4.3 Error in two-dimensional elastostatic plate models

While the single element case provides important insights into the local errors in a cut element, it is important to also evaluate the effects of integration error on the overall error in models more typical of those used in practice, where cut elements comprise only a subset of the finite element mesh, and cut elements interact with neighboring cut and un-cut elements.

To that end, two elastostatic models with known analytic solutions are examined as described below. The numerical approximation is obtained using the X-FEM with volume fraction strategy, as well as with moment fitting using four-point and six-point quadrature. All simulations in this paper were performed using the MOOSE (Multi-physics Object Oriented Simulation Environment) [21] framework, developed at Idaho National Laboratory.

4.3.1 Beam in bending

One quarter of a two dimensional beam in bending with a horizontal crack is modeled in the domain $[0, 1] \times [0, 1]$. Figure 10a shows the geometry and boundary conditions applied to this model. Displacements in the x directions are fixed on the left boundary (which is a symmetry plane). The bottom surface is the neutral axis of the beam, of which only the top portion is modeled. Assuming plane strain conditions, the exact displacement field is given by:

$$\begin{cases} u = -\frac{(1-\nu^2)M}{EI} xy, \\ v = \frac{(1-\nu^2)M}{2EI} \left[x^2 - 1 + \frac{\nu}{1-\nu} y^2 \right]. \end{cases} \quad (39)$$

The corresponding stress field is:

$$\begin{cases} \sigma_{xx} = -\frac{My}{I}, \\ \sigma_{yy} = \tau_{xy} = 0, \end{cases} \quad (40)$$

where M is the applied moment and I is the moment of inertia. Traction boundary conditions consistent with this stress field are applied to the right surface to obtain this bending behavior, and the top and bottom surface are traction-free. It is assumed here that $E = 10^6$, $\nu = 0.3$, $M = 2 \times 10^4$ and $I = 2/3$.

Since σ_{yy} and τ_{xy} are zero over the entire domain, a horizontal crack embedded in the plate is a traction-free surface, and adding it will not change the solution. Thus, the solution (39) for a two-dimensional plate without any crack still holds for the same plate embedded with a crack.

Uniform and irregular meshes are used in this simulation on each of the integration schemes studied here. A series of simulations were performed on meshes generated by

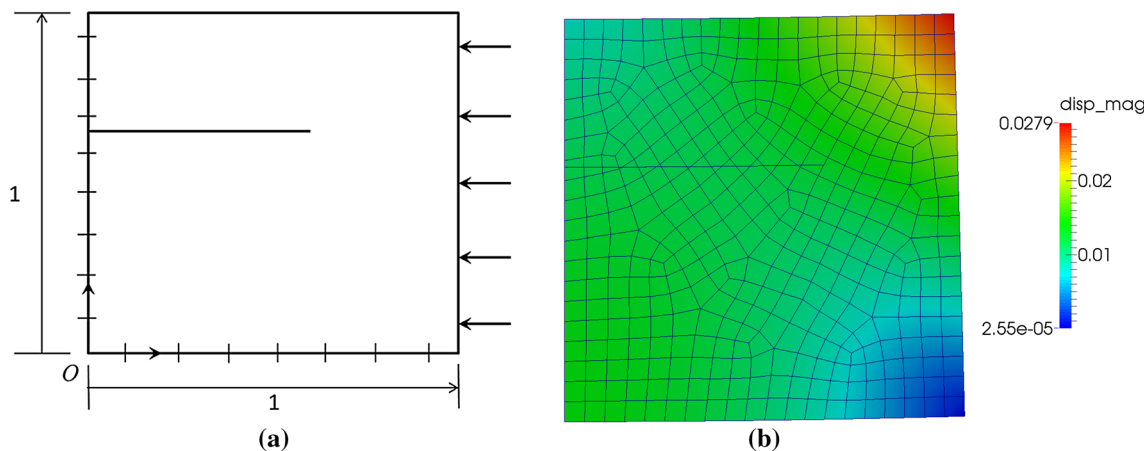


Fig. 10 **a** Geometry and boundary conditions of the bending beam problem. Dirichlet boundary conditions on u and v are imposed along the sides $x = 0$ and $y = 0$, respectively, while a traction boundary condition is specified for $x = 1$. **b** Displacement magnitude computed with the X-FEM with a six-point moment-fitting rule on the unstructured mesh

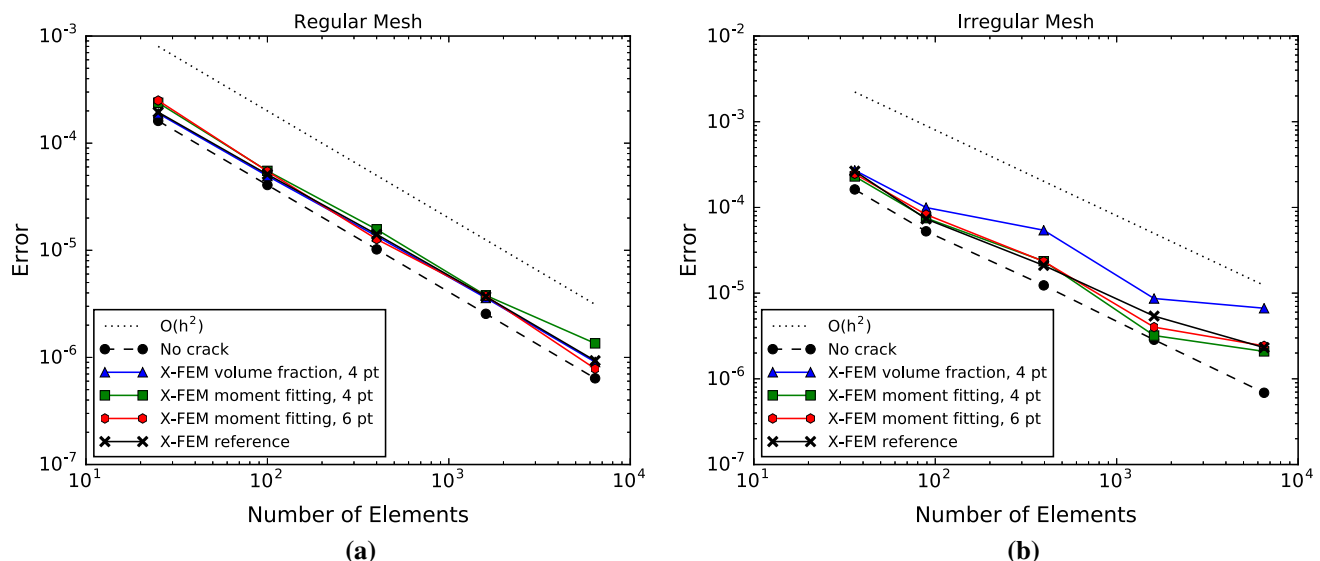


Fig. 11 Error decay for the cracked beam problem on **a** uniform meshes and **b** unstructured meshes. Results are shown for the X-FEM with moment fitting and volume fraction integration, in addition to a “reference” solution using a 19th order Gauss-Lobatto quadrature rule. “No crack” refers to a model of the beam using the same mesh as the X-FEM cases, but using standard elements and no crack

sequentially subdividing the elements in the original uniform and irregular meshes. The global error of the finite element approximations using various strategies is presented in Fig. 11. The error is defined in the L^2 sense as:

$$\text{error} = \sqrt{\int_{\Omega} (\mathbf{u}^h - \mathbf{u})^2 d\Omega} \quad (41)$$

where \mathbf{u}^h is the finite element approximation and \mathbf{u} is the exact solution.

From Fig. 11a it can be seen that for uniform meshes, all strategies have an optimal convergence rate, although the uncracked case consistently has slightly smaller errors than

the X-FEM cases. However, the advantage of the moment-fitting strategy is more pronounced for unstructured meshes, where both the four and six-point rules exhibit more uniform error decay than the volume fraction approach, which has higher errors and a convergence rate that is suboptimal.

Another interesting observation is that neither of the 4-point and 6-point rules exhibit superior accuracy, even though for a single element it was shown in Sect. 4.3 that the 6-point rule has generally smaller errors in element stiffness calculations. One potential reason for this is that the elements cut by the crack are only a small portion of the entire mesh, and thus the influence from these cut elements on the global error is limited. Another reason may be that the integration

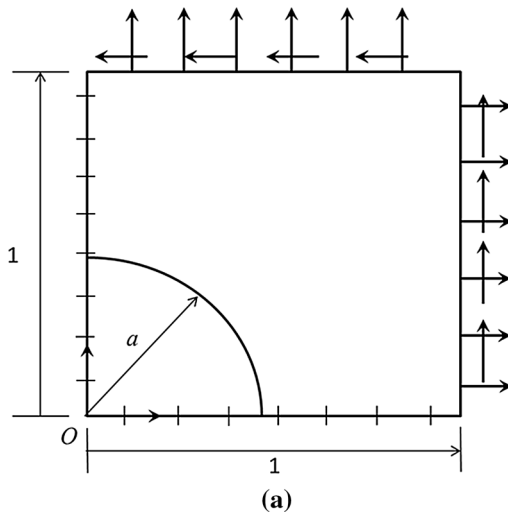
error is so small that it is overwhelmed by the discretization error.

Finally, further discussion of the X-FEM “reference” solutions in Fig. 11 is warranted. These solutions use a modified 19th order Gauss-Lobatto quadrature rule. It is a standard version of that scheme, except that the contributions from any integration points outside the physical domain are set to zero. Because there is a large number of integration points in each element, this provides a very good approximation of, but not an exact integration of the discontinuous function over the domain of partial elements. The errors and convergence rate for this “reference” scheme are very similar to those from the two moment-fitting schemes.

4.3.2 Plate with a circular hole

The strategy to assess convergence behavior in the previous example was also applied to a simulation of a square plate with a circular hole at the center, subjected to tractions on the plate boundaries. The geometry and boundary conditions of this problem, which is modeled using quarter symmetry, are shown in Fig. 12. We note that the hole geometry is represented with the X-FEM, so that partial elements are created along the hole boundary. Equations (42) and (43) are analytic solutions for the displacement and stress fields, written in polar coordinates [22]:

$$\begin{cases} u(r, \theta) = \frac{\sigma a}{8\mu} \left[\frac{r}{a}(\kappa + 1) \cos \theta + 2\frac{a}{r}((1 + \kappa) \cos \theta + \cos 3\theta) - 2\frac{a^3}{r^3} \cos 3\theta \right] \\ v(r, \theta) = \frac{\sigma a}{8\mu} \left[\frac{r}{a}(\kappa - 3) \sin \theta + 2\frac{a}{r}((1 - \kappa) \sin \theta + \sin 3\theta) - 2\frac{a^3}{r^3} \sin 3\theta \right] \end{cases} \quad (42)$$



(a)

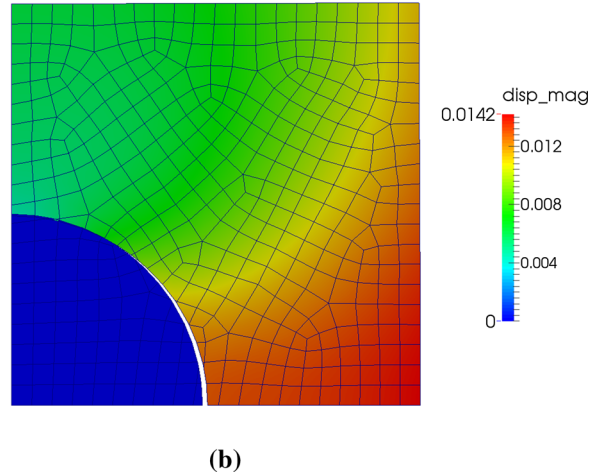


Fig. 12 **a** Geometry and boundary conditions of the plate with a hole. The radius $a = 0.4733$. Dirichlet boundary conditions on u and v are imposed along the sides $x = 0$ and $y = 0$, respectively, while traction boundary conditions are specified for $x = 1$ and $y = 1$. **b** The displacement magnitude computed with the X-FEM with the 6-point moment fitting rule using an unstructured mesh

$$\begin{cases} \sigma_{xx}(r, \theta) = \sigma \left[1 - \frac{a^2}{r^2} \left(\frac{3}{2} \cos 2\theta + \cos 4\theta \right) + \frac{3}{2} \frac{a^4}{r^4} \cos 4\theta \right] \\ \sigma_{yy}(r, \theta) = \sigma \left[-\frac{a^2}{r^2} \left(\frac{1}{2} \cos 2\theta - \cos 4\theta \right) - \frac{3}{2} \frac{a^4}{r^4} \cos 4\theta \right] \\ \tau_{xy}(r, \theta) = \sigma \left[-\frac{a^2}{r^2} \left(\frac{1}{2} \sin 2\theta + \sin 4\theta \right) + \frac{3}{2} \frac{a^4}{r^4} \sin 4\theta \right] \end{cases} \quad (43)$$

where $\kappa = 3 - 4\nu$. In the above, σ is a scale factor that represents the magnitude of the external force, and is set to 10^4 . Traction boundary conditions consistent with this stress field are applied to the upper and right surfaces of the model.

The error curves corresponding to the various integration strategies are given in Fig. 13. The decay rates of global error for all the strategies are optimal except the volume fraction strategy, whose error curve tends to be not as smooth but shows a slight super-convergent trend. However, based on experience with the other tests, this super-convergence rate is not a general phenomenon and can likely be attributed to the discretization of this specific model. The 4-point and 6-point rules with moment fitting both have errors that are very close to those from the fitted mesh and the X-FEM “reference” solution.

These results are very consistent with those for the cracked beam problem. The X-FEM models that employ moment fitting for integration give very low errors and optimal convergence rates. The X-FEM models that use the volume fraction strategy for integration are also a viable solution strategy, only with somewhat higher errors and lower convergence rates than what can be obtained with the moment fitting strategy.

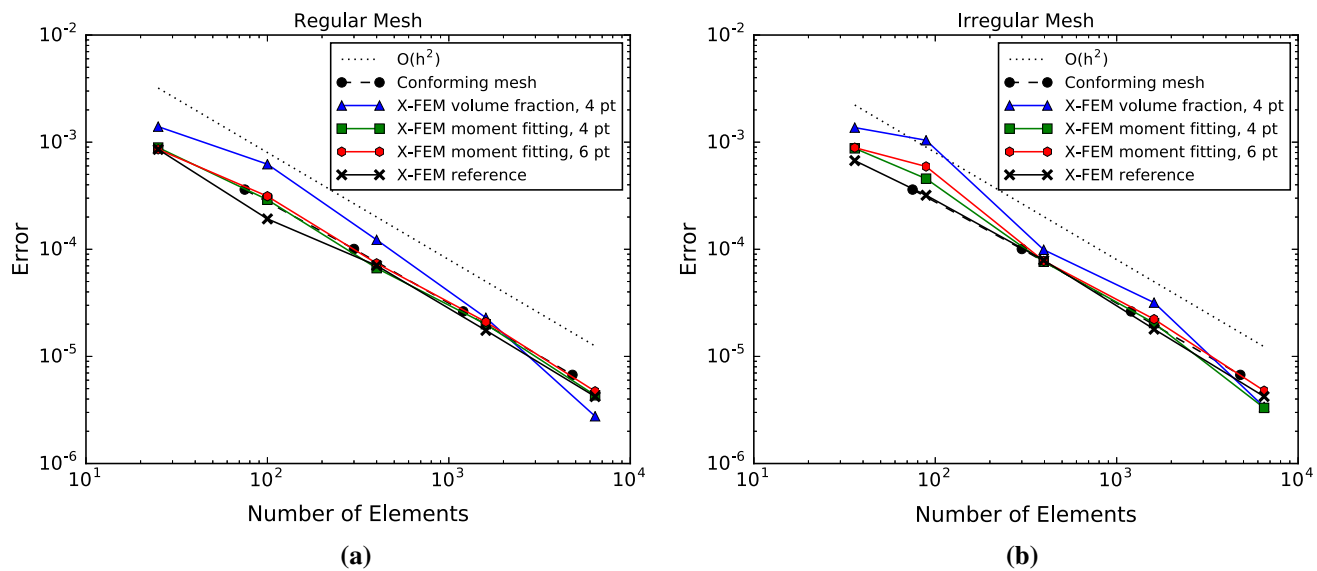


Fig. 13 Error decay for the plate with a hole problem on **a** uniform meshes and **b** unstructured meshes. Results are shown for the X-FEM with moment fitting and volume fraction integration, in addition to a “reference” solution using a 19th order Gauss-Lobatto quadrature rule. The “conforming mesh” results are from a standard finite element mesh that conforms to the geometry of the hole as shown in Fig. 12a

4.4 Crack propagation test with plasticity

A major motivation to use the moment fitting or volume fraction methods for integration of partial elements is to avoid the need to project history data from the original integration points to new integration points. When using state-dependent nonlinear constitutive models to describe bulk behavior, avoiding remapping material data greatly simplifies the X-FEM algorithm.

To demonstrate the behavior of the various integration techniques on a problem with state-dependent material, a simplified model of a crack propagating through a plastically deforming material has been developed. This problem consists of a square, two-dimensional plate with an initially-prescribed edge crack on the left side of the plate. The plate has dimensions of 25×25 , and the initial length of the crack is 5.5. The bottom surface of the plate is fixed against displacement in the vertical direction, the right side of the plate is fixed against displacement in the horizontal direction, and a monotonically-increasing vertical displacement is imposed at the top surface, putting the plate in tension in the vertical direction.

Criteria for the rate and direction of crack propagation would typically be based on the physical response. To aid in the comparison of results, however, the propagation of the crack was prescribed in the same way for the various modeling approaches considered in this problem. If t is the pseudo-time in this quasi-static analysis, which runs from $t = 0$ to $t = 1$, the prescribed vertical displacement, $d_y = 0.1t$. The crack is prescribed to grow in a horizontal path from the left to the right side of the model. Beginning at

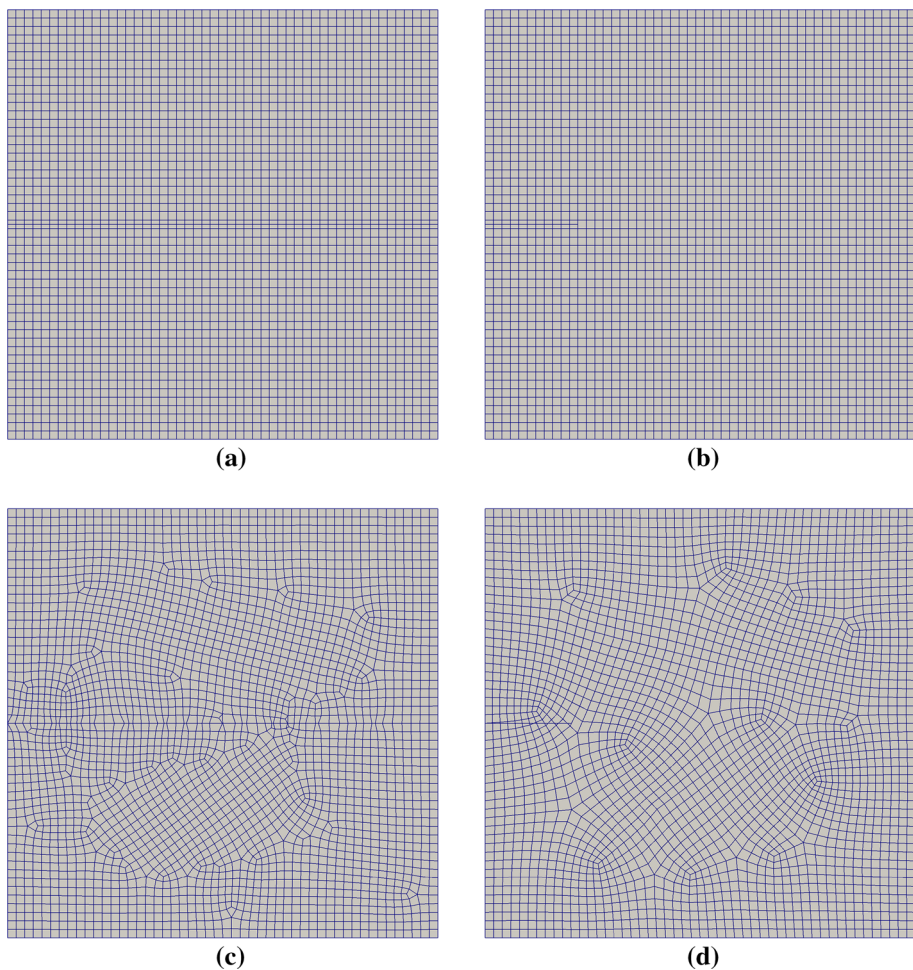
$t = 0.05$, the crack length, l_c , is prescribed to increase over time as $l_c = 5.5 + 20(t - 0.05)$, so that at the final time of the analysis, the crack is just short of propagating all the way through the body.

Four different modeling approaches are compared in this problem. For a reference result, the propagating crack is represented by the programmed release of nodes in a tied node-on-face contact interaction between the top and bottom halves of the domain. This is compared with three models using the X-FEM to represent crack propagation, and which use varying integration approaches: a four-point integration rule that uses the volume fraction, a four-point integration rule that uses moment fitting (with blended weights), and a six-point integration rule with moment fitting (also with blended weights).

These algorithms were employed on both regular and irregular meshes, shown in Fig. 14. Care was taken to ensure that the discretized location of the advancing crack tip was equivalent in the contact release and X-FEM cases. The irregular meshes were constructed to be reasonably equivalent in the contact release and X-FEM models. The nodes in the mesh used for the contact release approach were positioned so that they would have the same locations as the intersection points of the X-FEM cutting plane and the cut element edges. Note that the vertical size of the elements adjacent to the crack surface in the regular contact release mesh is half of all other elements. This is to permit a more direct comparison to the X-FEM tests, where the cut elements are split by a horizontal plane.

We note that without the use of blended weights, integration rules using moment fitting did not produce robust results

Fig. 14 Meshes used in study of crack propagating through a plastic body. **a** Regular mesh for reference contact release simulation. **b** Regular mesh for X-FEM simulations, showing initial prescribed crack. **c** Irregular mesh for reference contact release simulation. **d** Irregular mesh for X-FEM simulations, showing initial prescribed crack



for this problem. This was particularly true for the simulations using irregular meshes. In these instances, the standard moment-fitting rules quickly gave rise to negative weights, and fairly early in the simulations, a lack of convergence in the Newton iterations was observed. No such issues were observed using the blended weights.

Plane strain conditions were used in all models. The elasto-plastic J_2 material model with linear isotropic hardening described in Sect. 2.2 was employed here. This problem was run in a finite deformation setting, and employed the approach described in Sect. 3.3.1 for volumetric locking control. The material has elastic properties defined by $E = 10^6$ and $\nu = 0.3$. For plastic behavior, it has a yield stress $\sigma_y = 2000$, and hardening modulus $H = 10^4$.

Multiple metrics were used to compare the results from the modeling approaches used here. The first of these is the time history of the J-integral, which represents the strain energy release rate, and can be written in the following form:

$$J = - \int_A [w\delta_{ij} - \sigma_{ij}u_{i,1}]q_{,j} dA \quad (44)$$

where w is the strain energy density, 1 represents the direction of crack propagation and A is the area enclosed by a hoop-

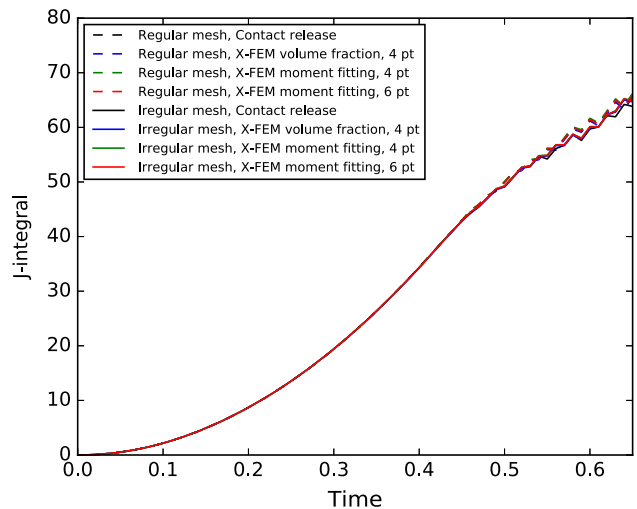
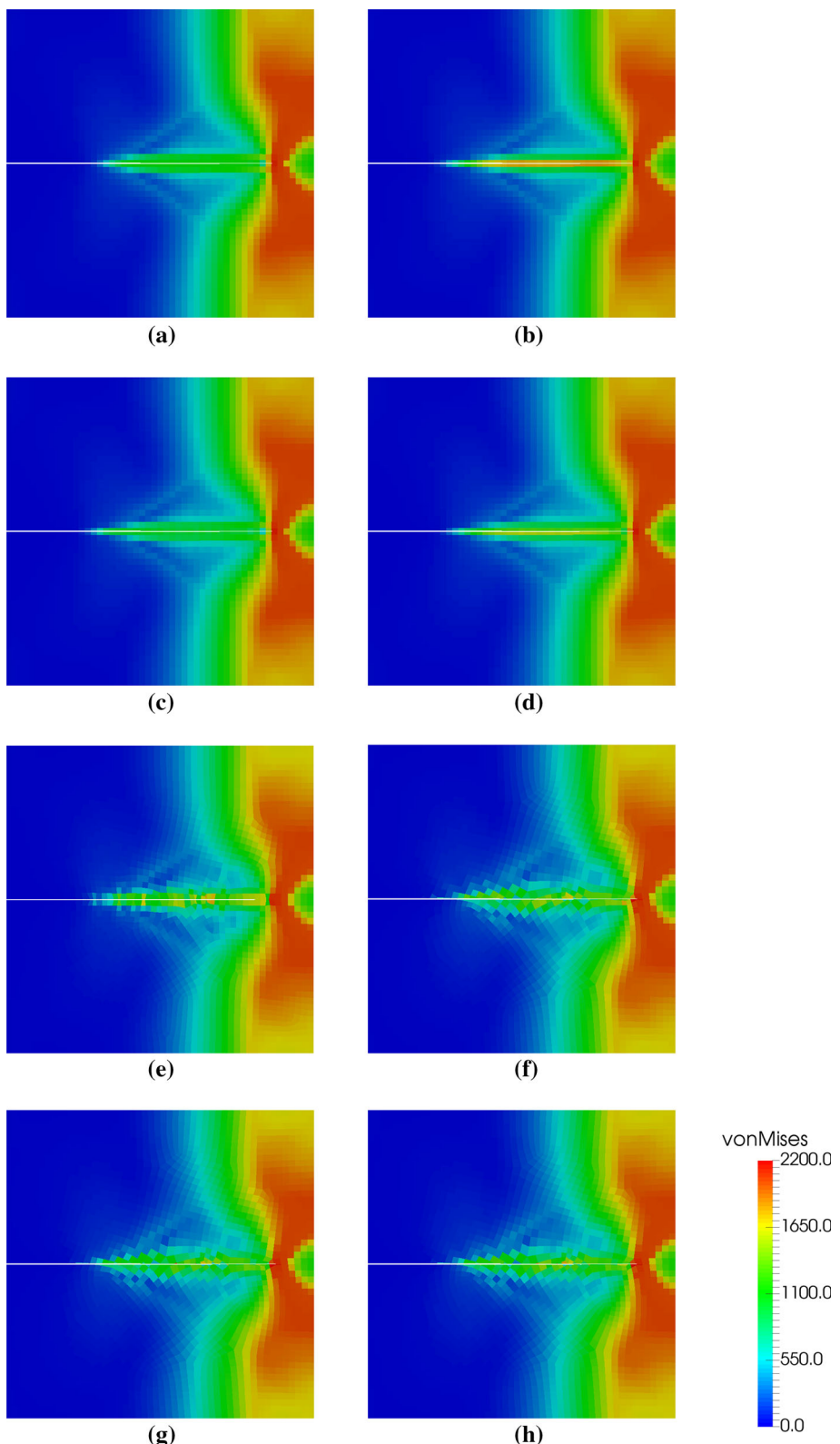


Fig. 15 Time history of J-integral for all cases. The outer radius used for evaluating the integral is 7 and inner radius 3. The J-integrals are only plotted before $t = 0.65$ because the outer boundary of the integration domain goes outside the problem domain after that time

shaped contour surrounding the crack tip. As can be seen in Fig. 15, there is very little difference in the J-integrals from the strategies used here. There is a small difference between

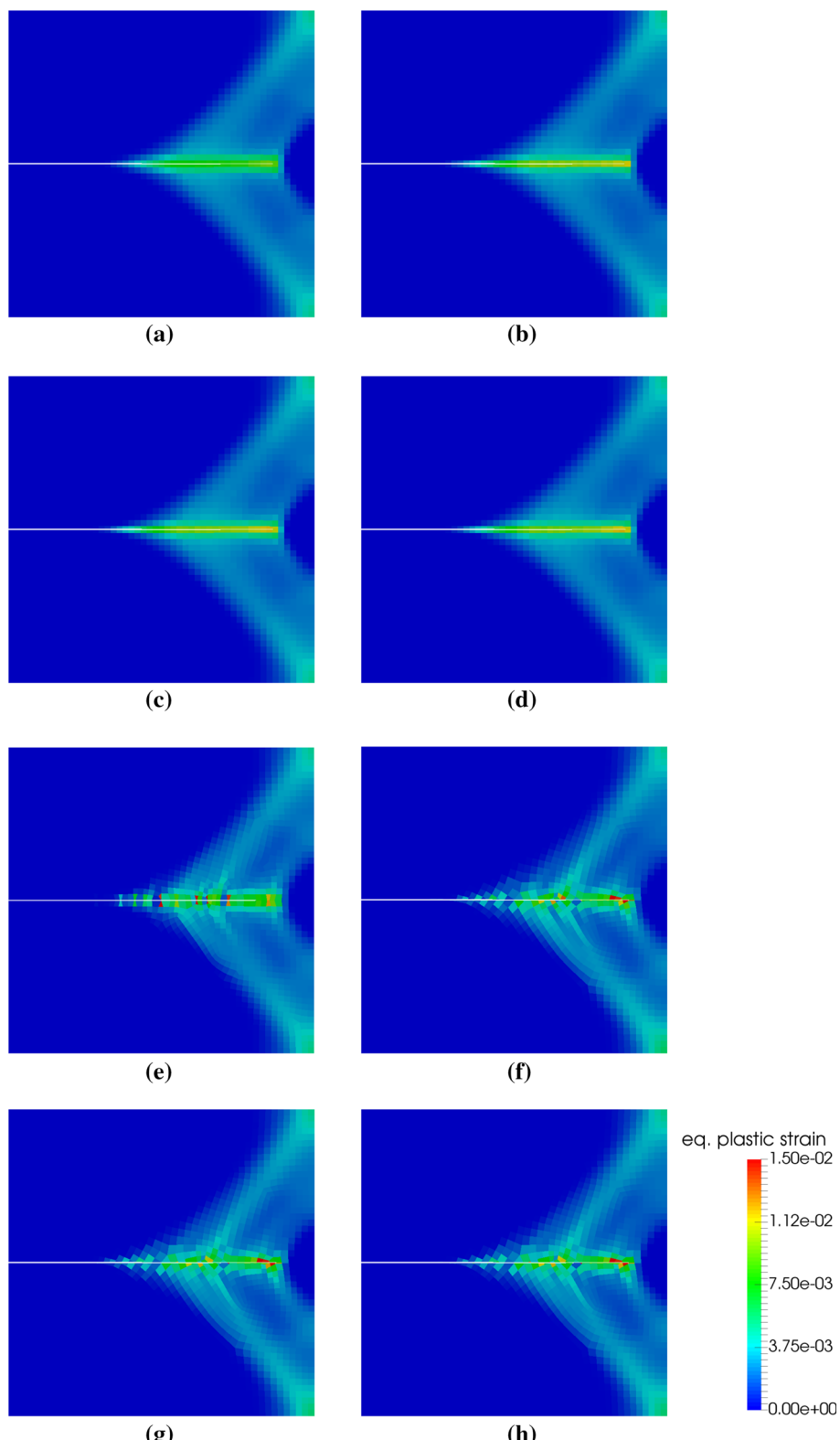
Fig. 16 Contour plots of von Mises stress for regular and irregular meshes at time $t = 0.9$. These are element-averaged quantities. **a** Contact release, regular mesh. **b** X-FEM, volume fraction, regular mesh. **c** X-FEM, 4 pt. moment fitting, regular mesh. **d** X-FEM, 6 pt. moment fitting, regular mesh. **e** Contact release, irregular mesh. **f** X-FEM, volume fraction, irregular mesh. **g** X-FEM, 4 pt. moment fitting, irregular mesh. **h** X-FEM, 6 pt. moment fitting, irregular mesh



the results for the irregular and regular meshes, but the results for the different computational methods for a given mesh type are very similar. There are noticeable oscillations in the

J-integral over time towards the end of the simulation, which are likely attributable to crack growth occurring in discrete increments through entire elements.

Fig. 17 Contour plots of equivalent plastic strain for regular and irregular meshes at time $t = 0.9$. These are element-averaged quantities. **a** Contact release, regular mesh. **b** X-FEM, volume fraction, regular mesh. **c** X-FEM, 4 pt. moment fitting, regular mesh. **d** X-FEM, 6 pt. moment fitting, regular mesh. **e** Contact release, irregular mesh. **f** X-FEM, volume fraction, irregular mesh. **g** X-FEM, 4 pt. moment fitting, irregular mesh. **h** X-FEM, 6 pt. moment fitting, irregular mesh



Contour plots of the von Mises stress and equivalent plastic strain obtained from the various modeling approaches are shown for the whole domain in Figs. 16 and 17, respectively. The results produced by the X-FEM models with the vari-

ous integration strategies are nearly indistinguishable from each other and from the reference contact release simulation for the regular mesh. As would be expected, there is some local noise in the results obtained using the irregular meshes,

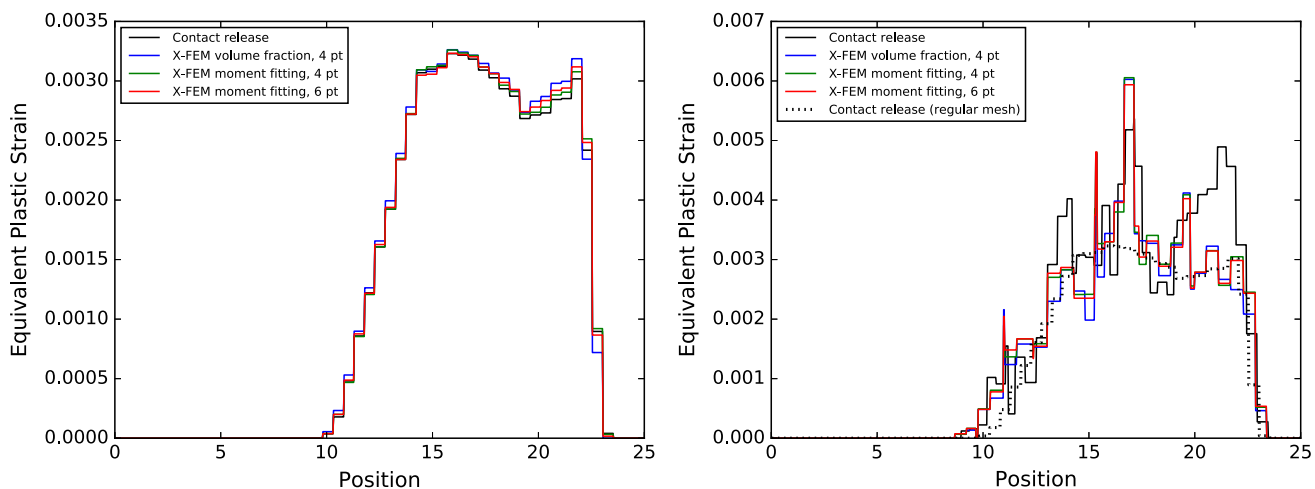


Fig. 18 Variation of equivalent plastic strain for the regular mesh (left) and irregular mesh (right) along a line offset a distance of 1 above the horizontal crack at time $t = 0.9$. These are element-averaged quantities. For reference, the contact release result for the regular mesh is also shown with the irregular mesh results

but overall, the finite element fields are very similar for all models.

To enable a more qualitative comparison between the results from the modeling approaches used here, plots of equivalent plastic strain along a line offset a distance of 1 (about 2 element widths) above the horizontal crack path are shown for the regular and irregular meshes in Fig. 18. From these plots, it can be seen that on the regular mesh, there is very little difference between the various approximations, although the X-FEM results that use moment fitting are slightly closer to the reference results than those obtained with volume fraction integration. The 4-point rule results in discrete fields slightly closer to the reference case than does the 6-point rule for most locations on that line, although the two moment fitting results are very close. This is counter-intuitive, but consistent with the results from the elasticity problems and single-element tests examined in this paper. In the fields generated using the irregular mesh, there is considerable noise in both the reference contact result and the X-FEM fields due to the nature of the mesh, making it difficult to draw any conclusions about the relative accuracy of these methods. The level of noise is roughly comparable in all cases.

The X-FEM approaches employing volume fraction and moment fitting methods for integration of partial elements all produce results that are all very comparable to the reference result when used on both regular and irregular meshes. All of these integration approaches simply copy stateful data from the original elements to the partial elements when they are split, and this problem demonstrates the viability of this approach for models with stateful material data. The moment fitting approaches are slightly more accurate than the volume fraction approach, although there is little perceivable advantage on practical problems with irregular meshes.

5 Conclusions

This work presented a simple integration scheme for use with X-FEM simulations of crack growth and materials with history-dependent material data. The scheme retains the location of quadrature points in elements as a crack evolves, such that history-dependent data can be trivially transferred from old to new discretizations as the crack geometry evolves. In contrast to earlier efforts, we explore a scheme that updates the weights of the quadrature points as the crack evolves, in order to improve accuracy. Our work demonstrates that standard moment-fitting schemes for this class of problems are insufficient, because the possibility of negative weights proves problematic, particularly for distorted elements. To remedy these issues, we proposed a simple formulation that blends moment-fitted weights with volume-fraction based weights, such that the all weights are strictly positive. This approach allows for positive weights that retain some of the accuracy of the moment-fitting. Importantly, the blended weights allow simulations of crack growth with plasticity to proceed with a level of accuracy that is largely indistinguishable from classical, fitted approaches using nodal release. Future work will focus on further improvements to schemes like this in order to improve accuracy and extend the method to three-dimensional problems.

Acknowledgements The bulk of the work presented in this manuscript was performed while first author Ziyu Zhang was a graduate research assistant in the Duke Computational Mechanics Laboratory. The support of Duke University is gratefully acknowledged. All authors would also like to acknowledge the support of the Idaho National Laboratory's Laboratory Directed Research and Development (LDRD) program (Project 13-071) and the Consortium for Advanced Simulation of Light Water Reactors (CASL), an Energy Innovation Hub under the U.S. Department of Energy. This manuscript has been authored by Battelle Energy Alliance, LLC under Contract No. DE-AC07-05ID14517 with

the U.S. Department of Energy. The United States Government retains and the publisher, by accepting the article for publication, acknowledges that the United States Government retains a nonexclusive, paid-up, irrevocable, world-wide license to publish or reproduce the published form of this manuscript, or allow others to do so, for United States Government purposes.

References

1. Moes N, Dolbow J, Belytschko T (1999) A finite element method for crack growth without remeshing. *Int J Numer Methods Eng* 46:131–150
2. Melenk JM, Babuška I (1996) The partition of unity finite element method: basic theory and applications. *Comput Methods Appl Mech Eng* 139:289–314
3. Belytschko T, Black T (1999) Elastic crack growth in finite elements with minimal remeshing. *Int J Numer Methods Eng* 45:601–620
4. Sukumar N, Dolbow JE, Moes N (2015) Extended finite element method in computational fracture mechanics: a retrospective examination. *Int J Fract* 196:189–206
5. Ventura G (2006) On the elimination of quadrature subcells for discontinuous functions in the extended finite-element method. *Int J Numer Methods Eng* 66:761–795
6. Natarajan S, Mahapatra DR, Bordas SPA (2010) Integrating strong and weak discontinuities without integration subcells and example applications in an XFEM/GFEM framework. *Int J Numer Methods Eng* 83:269–294
7. Chin EB, Lasserre JB, Sukumar N (2016) Modeling crack discontinuities without element-partitioning in the extended finite element method. *Int J Numer Methods Eng* 110:1021
8. Sudhakar Y, Wall WA (2013) Quadrature schemes for arbitrary convex/concave volumes and integration of weak form in enriched partition of unity methods. *Comput Methods Appl Mech Eng* 258:39–54
9. Elguedj T, Gravouil A, Combescure A (2006) On the elimination of quadrature subcells for discontinuous functions in the extended finite-element method. *Comput Methods Appl Mech Eng* 195:501–515
10. Liu X, Waisman H, Fish J (2012) A new crack tip enrichment function in the extended finite element method for general inelastic materials. *J Multiscale Comput Eng* 10:343–360
11. Martin A, Esnault JB, Massin P (2015) About the use of standard integration schemes for X-FEM in solid mechanics plasticity. *Comput Methods Appl Mech Eng* 283:551–572
12. Rashid MM (1993) Incremental kinematics for finite element applications. *Int J Numer Methods Eng* 36:3937–3956
13. Simo JC, Hughes TJR (1998) Computational inelasticity. Springer, New York
14. Richardson CL, Hegemann J, Sifakis E, Hellrunz J, Teran JM (2011) An X-FEM method for modeling geometrically elaborate crack propagation in brittle materials. *Int J Numer Methods Eng* 88:1042–1065
15. Lyness JN, Jespersen D (1975) Moderate degree symmetric quadrature rules for the triangle. *J Inst Math Appl* 15:19–32
16. Song JH, Areias PMA, Belytschko T (2006) A method for dynamic crack and shear band propagation with phantom nodes. *Int J Numer Methods Eng* 67:868–893
17. Wissmann JW, Becker T (1986) Partially symmetric cubature formulas for even degrees of exactness. *SIAM J Numer Anal* 23(3):676–685
18. Hughes TJR (1980) Generalization of selective integration procedures to anisotropic and nonlinear media. *Int J Numer Methods Eng* 15(9):1413–1418
19. Moran B, Ortiz M, Shih CF (1990) Formulation of implicit finite element methods for multiplicative finite deformation plasticity. *Int J Numer Methods Eng* 29(3):483–514
20. Mathworks I (2015b) MATLAB and statistics toolbox release 2014a. The MathWorks Inc., Natick
21. Gaston D, Newman C, Hansen G, Lebrun-Grandié D (2009) A parallel computational framework for coupled systems of nonlinear equations. *Nucl Eng Des* 239(10):1768–1778
22. Moumnaoui M, Belouettar J, Bechet E, Bordas S, Quoirin D, Potier-Ferry M (2011) Finite element analysis on implicitly defined domains: an accurate representation based on arbitrary parametric surfaces. *Comput Methods Appl Mech Eng* 200(5–8):774–796